Am J Transl Res 2025;17(7):5441-5452
www.ajtr.org /ISSN:1943-8141/AJTR0163464

Original Article

Development of a multimodal predictive model using PET/CT radiomics and clinical data for preoperative assessment of lymphovascular invasion in gastric cancer

Chunqiao Wu[1], Hongjie Hu[2], Fanger Bao[1], Zhiying Fei[1]

[1]Nursing Department, Sir Run Run Shaw Hospital, Zhejiang University School of Medicine, No. 3 Qingchun East Road, Shangcheng District, Hangzhou 310014, Zhejiang, China; [2]Radiology Department, Sir Run Run Shaw Hospital, Zhejiang University School of Medicine, No. 3 Qingchun East Road, Shangcheng District, Hangzhou 310014, Zhejiang, China

Received January 21, 2025; Accepted June 20, 2025; Epub July 15, 2025; Published July 30, 2025

Abstract: Objectives: To develop and validate a multimodal predictive model combining positron emission tomography/computed tomography (PET/CT) radiomic features with clinical data for the preoperative assessment of lymphovascular invasion (LVI) in patients with gastric cancer (GC). Methods: Between December 2017 and December 2022, 325 GC patients with pathologically confirmed LVI status were retrospectively enrolled. PET/CT scans were performed according to standard protocols, and 1,057 radiomic features were extracted from both imaging modalities following appropriate preprocessing. LASSO regression was used to select informative features for separate CT, PET, and combined PET/CT models. Key clinical variables - including age, maximum standardized uptake value, total lesion glycolysis, lymph node metastasis, and tumor grade - were integrated using multivariate logistic regression to construct a comprehensive predictive model. Model performance was assessed using ROC curve analysis. Diagnostic metrics - including AUC, sensitivity, specificity, accuracy, and Net Reclassification Improvement (NRI) - were calculated for each model. Results: The CT, PET, and combined PET/CT models achieved AUCs of 0.823, 0.761, and 0.861, respectively. The final multimodal model integrating PET/CT radiomics with clinical data demonstrated superior performance, with an AUC of 0.904, specificity of 91.91% and sensitivity of 74.07%. Independent predictors of LVI included age, SUVmax, TLG, and lymph node metastasis. NRI analysis showed a 10.35% improvement in risk classification compared to the PET/CT radiomic model alone. Conclusions: The multimodal predictive model demonstrated excellent diagnostic accuracy for preoperative assessment of LVI in GC patients and may support individualized treatment planning and risk stratification. Prospective multicenter studies are needed to further validate its clinical utility.

Keywords: Gastric cancer, radiomics, lymphovascular invasion, positron emission tomography/computed tomography, multimodal model

Introduction

Gastric cancer (GC) is among the most common and lethal malignancies worldwide [1]. According to recent statistics, GC ranks fifth in incidence and fourth in cancer-related mortality, with particularly high prevalence in East Asia [2]. Due to its aggressive behavior and heterogeneity, patient prognosis is closely tied to tumor staging. Approximately 80% of GC cases are diagnosed at an advanced stage, with median survival under 12 months for late-stage patients [3]. Although advances in neoadjuvant therapy, targeted therapy, and immunotherapy have been made, surgical resection combined with D2 lymphadenectomy remains the cornerstone of treatment [4]. Therefore, early diagnosis and accurate staging are essential for formulating effective treatment strategies and improving survival.

Lymphovascular invasion (LVI) is a critical pathologic feature of GC, indicative of tumor aggressiveness, metastatic potential, and overall prognosis [5]. Its presence is associated with poor clinical outcomes. However, current LVI diagnosis depends on postoperative histopathologic examination, which is invasive, time-

https://doi.org/10.62347/PBNU9406

consuming, and unsuitable for preoperative decision-making [6]. Thus, a non-invasive method for preoperatively predicting LVI would be highly valuable for guiding surgical planning, lymph node dissection, and adjuvant therapy selection.

With the development of advanced imaging and data analysis techniques, radiomics has emerged as a promising tool for extracting high-dimensional quantitative features from medical images to characterize tumor biology [7]. Radiomics enables the capture of tumor heterogeneity and microenvironmental information, offering novel opportunities for preoperative diagnosis and prognostic assessment in GC [8]. Positron emission tomography/computed tomography (PET/CT), which combines functional and anatomic imaging, is widely used in GC for staging, treatment monitoring, and recurrence detection [9]. Data such as metabolic tumor volume (MTV), maximum standardized uptake value (SUVmax), and total lesion glycolysis (TLG) provide valuable information on tumor metabolism and aggressiveness [10]. However, the diagnostic accuracy of PET or CT alone remains limited. For instance, PET/CT shows reduced sensitivity in certain GC subtypes, such as signet ring cell carcinoma, while CT has low resolution for detecting small metastatic lesions [11]. Therefore, integrating PET/CT radiomic features with clinical data into a multimodal predictive model represents a promising research direction.

This study aimed to develop a multimodal predictive model that combines PET/CT radiomic features with clinical variables using LASSO regression for feature selection. The goal is to accurately predict preoperative LVI status in GC patients, thereby aiding risk stratification and personalized treatment planning. The novelty of this study lies in the integration of radiomic and clinical data to improve interpretability and practicality. The model demonstrates strong predictive performance for clinical use to optimize individual management for GC patients.

Patients and methods

Patient information

This retrospective study was approved by the Ethics Committee of Sir Run Run Shaw Hospital, Zhejiang University School of Medicine. Due to data anonymization, the requirement for written informed consent was waived. 325 total GC patients with pathologically confirmed LVI diagnosed between December 2017 and December 2022 were included.

Inclusion and exclusion criteria

Inclusion criteria: 1. Preoperative PET/CT imaging performed. 2. LVI status confirmed by pathological examination of surgical specimens. 3. No prior radiotherapy, chemotherapy, or other antitumor treatments. 4. Complete clinical data available. 5. No severe organ dysfunction (e.g., cardiac, renal, or hepatic failure) prior to surgery. 6. No serious infections or immune system diseases that could affect imaging outcomes. 7. Imaging data met the quality requirements for radiomic analysis.

Exclusion criteria: 1. History of other malignancies. 2. Prior treatments or experimental therapies for other tumors. 3. Poor PET/CT image quality due to abnormal metabolism or severe obesity. 4. Postoperative pathology inconsistent with GC (e.g., mesenchymal tumor or lymphoma). 5. Non-standard image acquisition or preprocessing protocols.

Grouping criteria

LVI status was diagnosed through standard hematoxylin-eosin histologic evaluation and other methods, independently assessed by two pathologists. The patients were divided into an LVI-positive group (189 cases, 58.2%) and an LVI-negative group (136 cases, 41.8%). The LVI-positive group had tissue samples confirming lymphatic or vascular invasion, while no such invasion was found in the LVI-negative group.

Data collection

Baseline data were retrieved from the hospital's electronic medical records. Clinical information included: (1) Gender (categorical: male/female). (2) Lymph node metastasis (LNM, categorical: negative/positive). (3) Tumor grade (categorical: well/moderately/poorly differentiated). (4) Molecular subtype (categorical: undifferentiated/diffuse/mixed/intestinal); (5) T stage (categorical: T1/T2/T3/T4); (6) N stage (categorical: N0/N1/N2/N3); (7) M stage (categorical: M0/M1); (8) Clinical TNM stage (categorical: I/II/III/IV); (9) Age (continuous, years).

Laboratory data included serum levels of Cancer Antigen 125 (CA125), Cancer Antigen 19-9 (CA199) (both continuous, U/mL).

Imaging data from PET/CT included: SUVmax, SUVmean, MTV, TLG, and tumor thickness (all continuous). These datasets were used for comprehensive analysis of clinical, pathologic, and imaging characteristics.

PET/CT imaging procedure

All patients fasted for at least 6 hours before scanning, with blood glucose levels controlled below 11.0 mmol/L. PET/CT scans were performed using the Discovery VCT 64 PET/CT system (GE Healthcare, Milwaukee, USA). Following intravenous injection of ^18F-FDG at a dose of 3.78 MBq/kg, patients rested for approximately 60 minutes before imaging.

A whole-body CT scan was first performed with the following parameters: (1) Tube current: 140 mA; (2) Tube voltage: 140 kV; (3) Slice thickness: 3 mm; (4) Reconstruction interval: 3 mm; (5) Matrix size: 512×512.

Subsequently, PET images were acquired with a 2-minute acquisition per bed position. Image reconstruction was conducted using the 3D ordered-subset expectation maximization algorithm.

Image analysis

PET/CT images were independently reviewed by two radiologists (Reader 1: 10 years of experience; Reader 2: 15 years), both blinded to clinical and pathologic information. Regions of interest (ROIs) were delineated on axial PET images using proprietary software (PET VCAR, GE Healthcare, USA), and metabolic parameters such as SUVmax were measured using a 40% SUVmax threshold for ROI definition. Any discrepancies between the readers were resolved by consensus.

Tumor segmentation and radiomic feature extraction

PET and CT images were retrieved from the Picture Archiving and Communication System for tumor segmentation. Tumor regions were automatically segmented on both PET and CT images using LIFEx software based on a 40% SUVmax threshold and were further refined by the radiologists. To ensure reproducibility, 40 cases (20 LVI-positive and 20 LVI-negative) were randomly selected and segmented twice by both radiologists. Preprocessing steps included: 1. Resampling images to a voxel size of 1 mm^3. 2. Gray level discretization (CT: bin width =25; PET: bin width =0.1). 3. Denoising using a Gaussian filter.

A total of 1,057 radiomic features - including shape, texture, and first-order statistics - were extracted following the Image Biomarker Standardisation Initiative guidelines using an AI-based platform (Artificial Intelligence Kit, GE Healthcare).

Radiomic feature selection and model construction

All radiomic features were standardized using Z-score normalization. Multivariate logistic regression was used to identify variables associated with LVI. Lasso regression was then employed to select the most informative subset of radiomic features for model construction, yielding separate diagnostic models for CT, PET, and combined PET/CT data. A comprehensive multimodal model integrating PET/CT radiomics with clinical data was constructed through multivariate logistic regression. Model performance was assessed using area under the curve (AUC), sensitivity, specificity, and accuracy.

Outcome measurements

Primary outcome: Development of a multimodal predictive model for LVI using PET/CT radiomic features and clinical data.

Secondary outcomes: 1. Comparison of imaging parameters (SUVmax, SUVmean, MTV, TLG) and laboratory indicators (CA125, CA199) between LVI-positive and LVI-negative groups using the Mann-Whitney U test and logistic regression to identify clinical, laboratory, and imaging predictors of LVI. 2. Selection of radiomic features using Lasso regression for construction of a radiomic signature. 3. Evaluation of diagnostic performance of CT, PET, PET/CT, and multimodal models, and development of a nomogram incorporating clinical data, validated by ROC curve analysis. 4. Evaluation of the multimodal model's added value in LVI risk stratification through Net Reclassification Improvement (NRI) analysis.

Statistical analysis

All statistical analyses and visualizations were performed using R software (version 4.3.3). Continuous variables were expressed as mean ± standard deviation or median [interquartile range], as appropriate. Inter-group comparisons were conducted using independent samples t-tests for normally distributed data and Mann-Whitney U tests for non-normally distributed data. Categorical variables (frequencies and percentages) were compared using chi-square or Fisher's exact tests, depending on sample size. Differences in AUC between models were evaluated using the DeLong test. Multivariate logistic regression was used to identify independent predictors, and Lasso regression was applied for radiomic feature selection. Diagnostic performance was assessed via ROC curve analysis, reporting AUC, sensitivity, specificity, and accuracy. Improvement in risk stratification was quantified using NRI. All statistical tests were two-sided, with P<0.05 considered significant.

Results

Comparison of baseline features between LVI-positive and LVI-negative patients

Significant differences in clinical and imaging findings were observed between LVI-positive and LVI-negative patients. LVI-positive patients had a significantly higher incidence of LNM (P<0.001), higher tumor grade (P=0.006), and distinct distributions of molecular subtypes (P=0.036). Additionally, they were older on average (P=0.015). In terms of imaging features, LVI-positive patients exhibited significantly elevated SUVmax (P<0.001), SUVmean (P=0.003), and TLG (P<0.001), reflecting greater metabolic activity. No significant differences were found in sex, T, N, M stages, clinical TNM stage, CA125, CA199, or tumor thickness (all P>0.05; **Table 1**).

Multivariate analysis of factors associated with LVI positivity

Categorical clinical variables were numerically encoded (**Table 2**), and multivariate logistic regression was performed to identify independent predictors of LVI. The analysis revealed that age (P<0.001, OR=5.187, 95% CI: 2.437-11.681), SUVmax (P<0.001, OR=0.125, 95% CI: 0.064-0.232), TLG (P=0.001, OR=0.356, 95% CI: 0.192-0.652), LNM (P<0.001, OR =5.502, 95% CI: 2.792-11.288), tumor grade (P=0.043, OR=1.690, 95% CI: 1.021-2.832), and PET/CT model (P<0.001, OR=19.063, 95% CI: 5.501-99.417) were significant predictors of LVI. In contrast, SUVmean (P=0.262, OR=0.709, 95% CI: 0.388-1.294) and undifferentiated molecular subtype (P=0.135, OR=0.808, 95% CI: 0.609-1.067) were not significantly associated with LVI (**Table 3**).

Lasso regression-based feature selection for LVI diagnostic models

Lasso regression was applied to identify radiomic features for each model. The CT model retained 28 features, the PET model retained 14, and the combined PET/CT model selected 33 features (**Figure 1A-C**). The selected features and corresponding coefficients are detailed in Tables S1, S2, S3.

Construction of a multivariate model combining clinical data and PET/CT features

Multivariate logistic regression incorporating both clinical data and PET/CT radiomic features identified the following independent predictors of LVI: age (P<0.001, OR=6.089, 95% CI: 2.654-15.230), SUVmax (P<0.001, OR=0.133, 95% CI: 0.067-0.252), TLG (P=0.002, OR=0.372, 95% CI: 0.194-0.702), LNM (P<0.001, OR =4.959, 95% CI: 2.457-10.440), and PET/CT (P<0.001, OR=19.063, 95% CI: 5.501-99.417). Tumor grade approached significance (P= 0.060, OR=1.688, 95% CI: 0.986-2.943; **Table 4**).

Score distribution across diagnostic models

Score distributions between LVI-positive and LVI-negative groups were compared across different diagnostic models. Significant differences were observed in all models, including the PET (P<0.001), CT (P<0.001), PET/CT model (P<0.001), and PET/CT + clinical data models (P<0.001). In all cases, LVI-positive patients had significantly higher scores (**Table 5**).

Diagnostic performance of various models

Receiver operating characteristic (ROC) curve analysis was used to evaluate model performance. The PET/CT + clinical data model achieved the highest AUC of 0.904 (95% CI:

Table 1. Distribution of clinical and imaging factors in LVI-positive and LVI-negative patients

Clinical Factors	LVI-Positive Patients (n=189)	LVI-Negative Patients (n=136)	Statistic	*P*-value
Gender			0.701	0.402
Female	61 (32.28%)	38 (27.94%)		
Male	128 (67.72%)	98 (72.06%)		
Lymph Node Metastasis			50.71	<0.001
Negative	24 (12.7%)	66 (48.53%)		
Positive	165 (87.3%)	70 (51.47%)		
Tumour Grade			10.255	0.006
Well-Differentiated	6 (3.17%)	10 (7.35%)		
Moderately Differentiated	66 (34.92%)	65 (47.79%)		
Poorly Differentiated	117 (61.9%)	61 (44.85%)		
Molecular Subtype			8.524	0.036
Undifferentiated	56 (29.63%)	22 (16.18%)		
Diffuse	54 (28.57%)	42 (30.88%)		
Mixed	43 (22.75%)	36 (26.47%)		
Intestinal	36 (19.05%)	36 (26.47%)		
T Stage			4.286	0.232
T1	33 (17.46%)	33 (24.26%)		
T2	97 (51.32%)	70 (51.47%)		
T3	53 (28.04%)	27 (19.85%)		
T4	6 (3.17%)	6 (4.41%)		
N Stage			0.772	0.856
N0	49 (25.93%)	31 (22.79%)		
N1	83 (43.92%)	61 (44.85%)		
N2	43 (22.75%)	31 (22.79%)		
N3	14 (7.41%)	13 (9.56%)		
M Stage			2.72	0.099
M0	128 (67.72%)	80 (58.82%)		
M1	61 (32.28%)	56 (41.18%)		
Clinical TNM Stage			3.14	0.371
I	4 (2.12%)	2 (1.47%)		
II	71 (37.57%)	48 (35.29%)		
III	53 (28.04%)	30 (22.06%)		
IV	61 (32.28%)	56 (41.18%)		
Age (years)	62.639 ± 10.206	59.813 ± 10.297	-2.453	0.015
CA125 (U/mL)	15.54 [9.37, 21.46]	16.12 [9.29, 26.60]	1.574	0.115
CA199 (U/mL)	64.55 [29.29, 106.42]	70.31 [30.44, 113.61]	0.856	0.392
SUVmax	6.184 ± 2.237	8.938 ± 2.670	10.088	<0.001
Tumour Thickness (cm)	1.673 ± 0.592	1.685 ± 0.547	0.193	0.847
TLG (mL×SUV)	76.15 [48.87, 105.05]	103.80 ± 46.76	-5.111	<0.001
SUVmean	7.97 [4.95, 11.12]	9.69 [7.30, 11.75]	2.989	0.003
MTV (mL)	8.76 [5.24, 12.09]	8.64 [5.09, 11.45]	0.606	0.545

Note: LVI: Lymphovascular Invasion, CA125: Cancer Antigen 125, CA199: Cancer Antigen 19-9, SUVmax: Maximum Standardized Uptake Value, SUVmean: Mean Standardized Uptake Value, TLG: Total Lesion Glycolysis, MTV: Metabolic Tumor Volume, T Stage: Tumor Stage, N Stage: Node Stage, M Stage: Metastasis Stage, Clinical TNM Stage: Clinical Tumor-Node-Metastasis Stage.

Table 2. Variable coding table

Variable	Classification
Age (years)	<57.62=0, ≥57.62=1
SUVmax	<7.055=0, ≥7.055=1
TLG (mL×SUV)	<106.205=0, ≥106.205=1
SUVmean	<8.045=0, ≥8.045=1
Lymph Node Metastasis	Negative =0, Positive =1
Tumor Grade	Well-Differentiated =1, Moderately Differentiated =2, Poorly Differentiated =3
Undifferentiated Type	Undifferentiated =1, Diffuse =2, Mixed =3, Intestinal =4
LVI	Negative =0, Positive =1

Note: LVI: Lymphovascular Invasion, SUVmean: Mean Standardized Uptake Value, TLG: Total Lesion Glycolysis, Clinical TNM Stage: Clinical Tumor-Node-Metastasis Stage.

Table 3. Multivariate logistic regression analysis for diagnostic variables of LVI

Variable	β Value	SE	*P*-value	OR Value	Lower	Upper
Age	1.646	0.397	<0.001	5.187	2.437	11.681
SUVmax	-2.081	0.326	<0.001	0.125	0.064	0.232
TLG	-1.033	0.311	0.001	0.356	0.192	0.652
SUVmean	-0.344	0.307	0.262	0.709	0.388	1.294
Lymph Node Metastasis	1.705	0.355	<0.001	5.502	2.792	11.288
Tumor Grade	0.525	0.259	0.043	1.69	1.021	2.832
Undifferentiated Type	-0.213	0.143	0.135	0.808	0.609	1.067

Note: LVI: Lymphovascular Invasion, SUVmean: Mean Standardized Uptake Value, TLG: Total Lesion Glycolysis, Clinical TNM Stage: Clinical Tumor-Node-Metastasis Stage.

0.873-0.935), outperforming the PET (AUC =0.761, 95% CI: 0.709-0.812), CT (AUC=0.823, 95% CI: 0.778-0.867), and PET/CT models (AUC=0.861, 95% CI: 0.822-0.901). This model also demonstrated the best sensitivity, specificity, Youden index, and accuracy (**Table 6**). DeLong test results confirmed statistically significant differences in AUCs between the PET model and all other models (P<0.05), and between the CT and PET/CT models (P=0.005). The PET/CT + clinical model was significantly superior to all others (P<0.05; **Table 7** and **Figure 2**).

NRI of the PET/CT + clinical model

NRI analysis demonstrated that the PET/CT + clinical model improved risk stratification by an overall rate of 10.35% (NRI=0.1035) compared to the PET/CT-only model. Specifically, the improvement was 3.26% (NRI+ =0.0326) for LVI-positive cases and 7.09% (NRI- =0.0709) for LVI-negative controls. In the LVI-positive group, 20.11% of patients were reclassified into higher-risk categories and 16.85% into lower-risk categories. In the LVI-negative group, 29.08% were reclassified to lower-risk and 21.99% to higher-risk categories. These results suggest that the new model significantly enhanced risk differentiation, particularly among LVI-negative patients (**Figure 3**).

Discussion

This study aimed to develop and validate a multimodal predictive model incorporating PET/CT radiomic features and clinical data to preoperatively assess LVI status in patients with GC. A retrospective analysis of 325 patients with pathologically confirmed GC and documented LVI status demonstrated that the multimodal model - integrating PET/CT radiomic features with clinical variables - achieved excellent diagnostic performance, with an AUC of 0.904. This significantly outperformed the single-modality models, including PET (AUC=0.761), CT (AUC=0.823), and combined PET/CT (AUC =0.861). Furthermore, the multimodal model yielded a NRI of 10.35%, highlighting its potential clinical value in LVI risk stratification.

Multivariate logistic regression identified age, SUVmax, TLG, and LNM as independent predic-

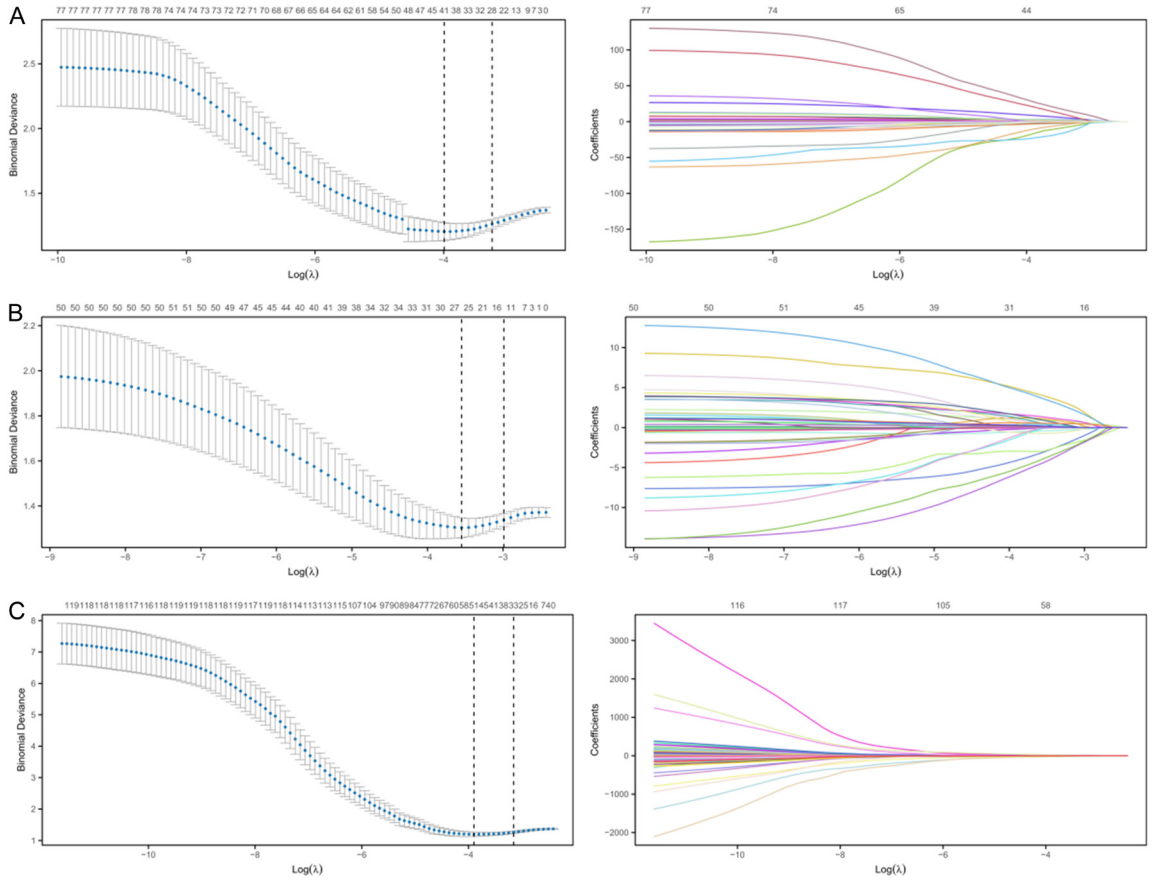

Figure 1. Selection process of feature variables for CT, PET, and CT + PET models based on Lasso regression. A. CT Model Lasso Regression Selection Process: The left graph shows the variation in cross-validation error, and the right graph displays the path of regression coefficients for each variable, resulting in the selection of 28 feature variables. B. PET Model Lasso Regression Selection Process: The left graph shows the variation in cross-validation error, and the right graph displays the path of regression coefficients for each variable, resulting in the selection of 14 feature variables. C. CT + PET Combined Model Lasso Regression Selection Process: The left graph shows the variation in cross-validation error, and the right graph displays the path of regression coefficients for each variable, resulting in the selection of 33 feature variables. Note: CT: Computed Tomography, PET: Positron Emission Tomography, CT + PET: Combined Computed Tomography and Positron Emission Tomography, LASSO: Least Absolute Shrinkage and Selection Operator.

tors of LVI, reinforcing their potential for roles in the pathogenesis and progression of LVI in GC.

In recent years, radiomics has gained increasing attention for its utility in GC diagnosis and prognostic evaluation. Prior studies have demonstrated that PET/CT-derived parameters such as SUVmax, MTV, and TLG, are valuable for assessing tumor metabolism and invasiveness. Integrating radiomic features with clinical data has been shown to enhance LVI prediction accuracy [12]. For example, Chen et al. [13] found that contrast-enhanced CT-based radiomics effectively predicted LVI status in GC. However, single-modality imaging approaches, such as PET-only or CT-only, have inherent limitations in sensitivity and specificity [14, 15].

This study addressed these limitations by combining PET and CT radiomic features with clinical data to construct a multimodal model, thereby improving prediction accuracy. Although consistent with findings from other multimodal radiomics research, this study is distinct in several respects - including the large number of features extracted, the application of Lasso regression for dimensionality reduction, and the model's enhanced clinical interpretability and feasibility.

The multimodal model capitalizes on the complementary strengths of PET and CT imaging. PET provides quantitative metrics of tumor metabolism (e.g., SUVmax and TLG), which reflect proliferative activity and glycolytic rate,

Table 4. Multivariate analysis of clinically significant variables combined with PET/CT for constructing LVI diagnostic model

Variable	β Value	SE	*P*-value	OR Value	Lower	Upper
Age	1.807	0.443	<0.001	6.089	2.654	15.23
SUVmax	-2.02	0.338	<0.001	0.133	0.067	0.252
TLG	-0.989	0.327	0.002	0.372	0.194	0.702
Lymph Node Metastasis	1.601	0.367	<0.001	4.959	2.457	10.44
Tumor Grade	0.523	0.278	0.06	1.688	0.986	2.943
PET/CT	2.948	0.72	<0.001	19.063	5.501	99.417

Note: PET/CT: Positron emission tomography/computed tomography, LVI: Lymphovascular Invasion, SUVmean: Mean Standardized Uptake Value, TLG: Total Lesion Glycolysis, Clinical TNM Stage: Clinical Tumor-Node-Metastasis Stage.

Table 5. Comparison of score distributions between LVI-positive and LVI-negative patients across different models

Variable	LVI-Positive Patients (n=189)	LVI-Negative Patients (n=136)	Statistic	*P*-value
PET	0.40 [0.28, 0.56]	0.24 [0.08, 0.33]	8.021	<0.001
CT	0.54 [0.26, 0.86]	0.08 [-0.18, 0.25]	9.931	<0.001
PET/CT	0.58 [0.30, 0.86]	-0.02 [-0.22, 0.23]	11.11	<0.001
PET/CT + Clinical Data	6.52 [4.56, 7.51]	2.68 ± 1.63	12.423	<0.001

Note: PET/CT: Positron emission tomography/computed tomography. Clinical Data (Age, SUVmax, TLG, Lymph Node Metastasis).

Table 6. Diagnostic performance of various models

Marker	AUC	CI Lower-Upper	Specificity	Sensitivity	Youden Index	Cut-off	Accuracy	Precision	F1 Score
PET	0.761	0.709-0.812	76.47%	65.08%	41.55%	0.341	69.85%	65.08%	71.51%
CT	0.823	0.778-0.867	77.21%	75.13%	52.34%	0.264	76.00%	75.13%	78.45%
PET/CT	0.861	0.822-0.901	86.03%	71.96%	57.99%	0.354	77.85%	71.96%	79.07%
PET/CT + Clinical Data	0.904	0.873-0.935	91.91%	74.07%	65.99%	4.666	81.54%	74.07%	82.35%

Note: PET/CT: Positron emission tomography/computed tomography. Clinical Data (Age, SUVmax, TLG, Lymph Node Metastasis).

Table 7. Comparative analysis of AUC differences between diagnostic models

Marker1	Marker2	Z-value	*P*-value	AUC Difference	CI Lower-Upper
PET	CT	-1.998	0.046	-0.062	-0.122
PET	PET/CT	-4.469	<0.001	-0.1	-0.088
PET	PET/CT + Clinical Data	-5.115	<0.001	-0.143	-0.11
CT	PET/CT	-2.777	0.005	-0.038	-0.054
CT	PET/CT + Clinical Data	-3.394	<0.001	-0.081	-0.094
PET/CT	PET/CT + Clinical Data	-2.018	0.044	-0.043	-0.083

Note: PET/CT: Positron emission tomography/computed tomography. Clinical Data (Age, SUVmax, TLG, Lymph Node Metastasis).

while CT offers detailed anatomic and morphologic information (e.g., tumor shape, volume, and boundary characteristics). By integrating these data sources, the model delivers a more comprehensive characterization of tumor biology and the tumor microenvironment, ultimately enhancing the accuracy of preoperative LVI prediction.

This study identified age as an important independent predictor of LVI, with older patients being more susceptible. This may be attributed to age-related declines in immune function, alterations in the tumor microenvironment, and changes in the expression of genes associated with tumor progression. Tumor cells in older individuals may exhibit greater invasiveness,

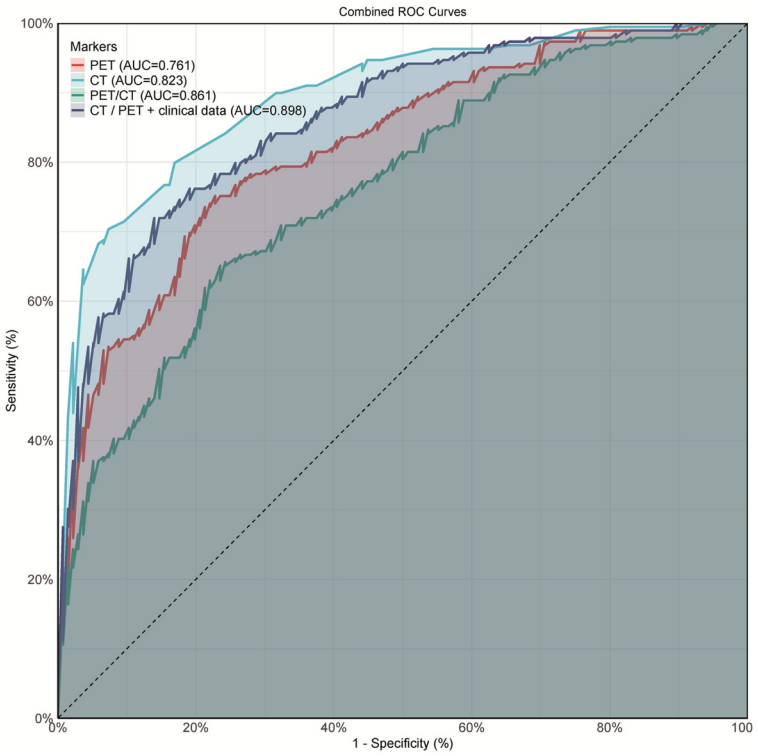

Figure 2. ROC curves and AUC comparison of various predictive models. Note: ROC: Receiver Operating Characteristic, AUC: Area Under the Curve, CT: Computed Tomography, PET: Positron Emission Tomography, PET/CT: Combined Computed Tomography and Positron Emission Tomography. Clinical Data (Age, SUVmax, TLG, Lymph Node Metastasis).

increasing their propensity to infiltrate vascular and lymphatic structures [16-18].

Interestingly, SUVmax, which reflects the tumor's highest metabolic activity, was inversely associated with LVI positivity. This suggests that tumors with lower metabolic activity may have a higher tendency for lymphatic dissemination [19]. While this finding contrasts with certain prior studies, it highlights the heterogeneity of tumor biology and warrants further investigation. One possible explanation is that a low SUVmax may indicate reduced proliferation but enhanced potential for invasion through alternative mechanisms, such as epithelial-mesenchymal transition (EMT).

TLG, a composite measure of MTV and mean SUV, reflects the tumor's overall metabolic burden [20]. This study found that lower TLG values were also associated with LVI positivity, supporting the notion that tumors with lower metabolic activity may still exhibit high invasive and metastatic potential. Some studies suggest that such tumors may leverage alternative invasion pathways, including EMT, to promote LVI [21].

Additionally, Kim et al. [22] reported that endoscopic features - such as tumor morphology and surface color changes - can serve as valuable predictors of LVI. Lin et al. [23], through an international multicenter study, developed a predictive model based on preoperative factors for assessing LVI and LNM, underscoring the importance of multimodal integration for clinical prediction.

LNM is a crucial clinical indicator of LVI, reflecting tumor aggressiveness and metastatic potential. Patients with LNM are more likely to exhibit LVI. Oh et al. [24] identified tumor size, depth of invasion, and histologic type as significant predictors of LNM, independent of LVI status. Meanwhile, studies by Xue et al. [25] and Zhu et al. [26] using PET-CT and machine learning models have demonstrated the potential of advanced imaging for LVI and LNM prediction, supporting the multimodal approach adopted in this study. Similarly, Xue et al. [27] showed that combining radiomic features with traditional clinical indicators significantly improves LNM prediction accuracy. Ge et al. [28] validated the role of multimodal radiomics using spectral CT and machine learning techniques, in line with our findings.

The multimodal predictive model developed in this study exhibited high diagnostic accuracy in preoperatively assessing LVI status in GC patients and offers substantial clinical utility. It may aid clinicians in surgical planning, including determining resection margins and guiding lymphadenectomy, possibly reducing surgical trauma and recurrence. Moreover, the model facilitates early identification of high-risk patients, enabling individualized adjuvant therapies such as chemotherapy, radiotherapy, or targeted treatment. Preoperative LVI prediction also provides prognostic insights and informs

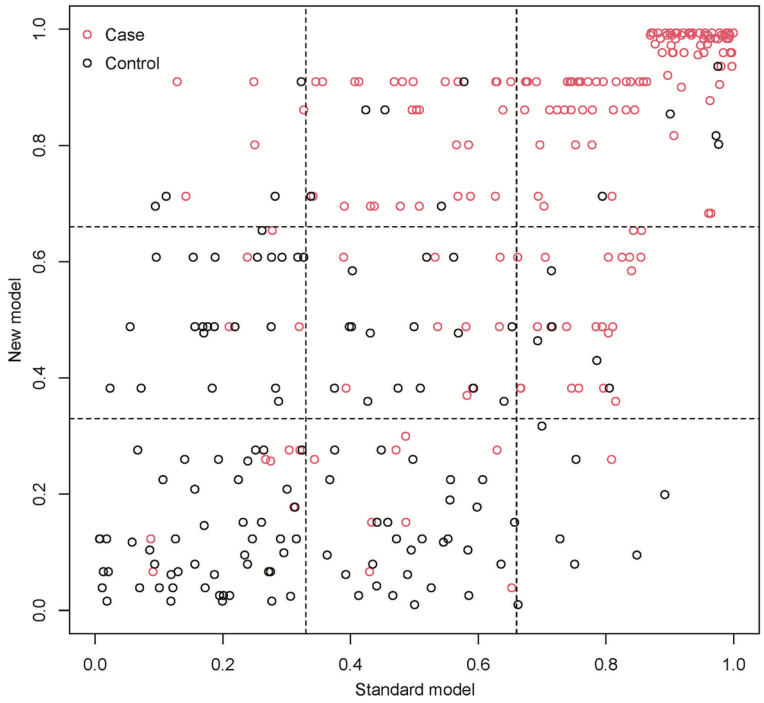

Figure 3. Risk reclassification performance of the new and old models. Note: The scatter plot illustrates the distribution of classification probabilities for the new model (PET/CT + clinical data) and the old model (PET/CT) in both case and control groups. The new model demonstrates more pronounced risk reclassification improvements in the control group.

follow-up strategies, allowing for timely detection of recurrence or metastasis.

The implementation of PET/CT radiomic analysis is feasible in clinical settings, leveraging existing imaging platforms and standardized workflows. The use of automated image acquisition and feature extraction tools supports seamless integration into clinical practice. Furthermore, incorporating electronic medical record data enhances workflow efficiency and enables real-time prediction to support personalized treatment decisions.

This study has several strengths. The relatively large sample size (n=325) enhances the statistical power and reliability of the findings. The integration of PET/CT radiomic features with clinical data improved predictive performance by leveraging complementary information sources. The application of Lasso regression for high-dimensional feature selection reduced model complexity while maintaining interpretability. Diagnostic performance was rigorously evaluated through ROC analysis and AUC comparison.

Nonetheless, limitations exist. The retrospective single-center design may have introduced selection bias and limit generalizability. The absence of external validation may constrain broader applicability. Additionally, reliance on specific software for radiomic feature extraction may have introduced methodological variability. Differences in imaging protocols, patient populations, and data processing could have contributed to inconsistencies across studies.

Future research should address these limitations through prospective, multicenter validation and explore the integration of radiomics with other biomarkers, such as genomics and proteomics, to enhance model robustness and predictive accuracy.

In conclusion, this study developed a multimodal predictive model combining PET/CT radiomic features with clinical data, demonstrating strong diagnostic performance in preoperative LVI assessment among GC patients. The model holds significant clinical potential in guiding personalized treatment and improving patient outcome.

Disclosure of conflict of interest

None

Address correspondence to: Chunqiao Wu, Nursing Department, Sir Run Run Shaw Hospital, Zhejiang University School of Medicine, No. 3 Qingchun East Road, Shangcheng District, Hangzhou 310014, Zhejiang, China. E-mail: wuchunqiao2024@163.com

References

[1] Li J, Wang L, Hu W, Wu J, Chen H, Wang L, Lv B, Zhang X, Dai Y, Huang Z, Cai Z, Ding X, Ye L, Ding J, Xiang L, Ye B, Chen S and Si J. Effect of premedication with pronase before upper gastrointestinal endoscopy: a multicenter prospective randomized controlled study. J Clin Gastroenterol 2024; 58: 53-56.

[2] Bray F, Laversanne M, Sung H, Ferlay J, Siegel RL, Soerjomataram I and Jemal A. Global cancer statistics 2022: GLOBOCAN estimates of incidence and mortality worldwide for 36 cancers in 185 countries. CA Cancer J Clin 2024; 74: 229-263.

[3] Lu G, Cai Z, Jiang R, Tong F, Tu J, Chen Y, Fu Y, Sun J and Zhang T. Reduced expression of E-cadherin correlates with poor prognosis and unfavorable clinicopathological features in gastric carcinoma: a meta-analysis. Aging (Albany NY) 2024; 16: 10271-10298.

[4] Shah MA, Kennedy EB, Alarcon-Rozas AE, Alcindor T, Bartley AN, Malowany AB, Bhadkamkar NA, Deighton DC, Janjigian Y, Karippot A, Khan U, King DA, Klute K, Lacy J, Lee JJ, Mehta R, Mukherjee S, Nagarajan A, Park H, Saeed A, Semrad TJ, Shitara K, Smyth E, Uboha NV, Vincelli M, Wainberg Z and Rajdev L. Immunotherapy and targeted therapy for advanced gastroesophageal cancer: ASCO guideline. J Clin Oncol 2023; 41: 1470-1491.

[5] Takano K, Ashikari K, Tamura S, Misawa N, Takatsu T, Yoshihara T, Nonaka T, Arimoto J, Sakamoto A, Chiba H, Fujii S, Nakajima A and Higurashi T. Clinicopathological features of endoscopically treated early gastric cancer with lymphovascular infiltration. J Cancer Res Clin Oncol 2023; 149: 5781-5790.

[6] Wu L, Liang Y, Zhang C, Wang X, Ding X, Huang C and Liang H. Prognostic significance of lymphovascular infiltration in overall survival of gastric cancer patients after surgery with curative intent. Chin J Cancer Res 2019; 31: 785-796.

[7] Chen Q, Zhang L, Liu S, You J, Chen L, Jin Z, Zhang S and Zhang B. Radiomics in precision medicine for gastric cancer: opportunities and challenges. Eur Radiol 2022; 32: 5852-5868.

[8] Xue Y, Zhang H, Zheng Z, Liu X, Yin J and Zhang J. Predictive performance of radiomics for peritoneal metastasis in patients with gastric cancer: a meta-analysis and radiomics quality assessment. J Cancer Res Clin Oncol 2023; 149: 12103-12113.

[9] Lin R, Lin Z, Chen Z, Zheng S, Zhang J, Zang J and Miao W. [(68)Ga]Ga-DOTA-FAPI-04 PET/CT in the evaluation of gastric cancer: comparison with [(18)F]FDG PET/CT. Eur J Nucl Med Mol Imaging 2022; 49: 2960-2971.

[10] Iwasa H, Nagamachi S, Nakayama S, Yamamoto T and Yoshimitsu K. The reproducibility of MTV and TLG of soft tissue tumors calculated by FDG-PET: comparison between the lower limit by the fixed value SUV 2.5 and that value by 30% of SUVmax. Jpn J Radiol 2023; 41: 531-540.

[11] Alakus H, Batur M, Schmidt M, Drebber U, Baldus SE, Vallböhmer D, Prenzel KL, Metzger R, Bollschweiler E, Hölscher AH and Mönig SP. Variable 18F-fluorodeoxyglucose uptake in gastric cancer is associated with different levels of GLUT-1 expression. Nucl Med Commun 2010; 31: 532-538.

[12] Wang P, Chen K, Han Y, Zhao M, Abiyasi N, Peng H, Yan S, Shang J, Shang N and Meng W. Prediction model based on radiomics and clinical features for preoperative lymphovascular invasion in gastric cancer patients. Future Oncol 2023; 19: 1613-1626.

[13] Chen X, Yang Z, Yang J, Liao Y, Pang P, Fan W and Chen X. Radiomics analysis of contrast-enhanced CT predicts lymphovascular invasion and disease outcome in gastric cancer: a preliminary study. Cancer Imaging 2020; 20: 24.

[14] Abbasian Ardakani A, Bureau NJ, Ciaccio EJ and Acharya UR. Interpretation of radiomics features-a pictorial review. Comput Methods Programs Biomed 2022; 215: 106609.

[15] Ma T, Zhang Y, Zhao M, Wang L, Wang H and Ye Z. A machine learning-based radiomics model for prediction of tumor mutation burden in gastric cancer. Front Genet 2023; 14: 1283090.

[16] Chen H, Chen Y, Dong Y, Gou L, Hu Y, Wang Q, Li G, Li S and Yu J. (18)F-FDG PET/CT radiomics-based multimodality fusion model for preoperative individualized noninvasive prediction of peritoneal metastasis in advanced gastric cancer. Ann Surg Oncol 2024; 31: 6017-6027.

[17] Xue XQ, Yu WJ, Shao XL, Li XF, Niu R, Zhang FF, Shi YM and Wang YT. Radiomics model based on preoperative 18F-fluorodeoxyglucose PET predicts N2-3b lymph node metastasis in gastric cancer patients. Nucl Med Commun 2022; 43: 340-349.

[18] Li Y, Huang L, Li L, Chen L, Chen P and Chen X. The evaluation of gastric cancer lymphovascular invasion using CT volume perfusion. Discov Med 2024; 36: 2037-2045.

[19] He Y, Yang M, Hou R, Ai S, Nie T, Chen J, Hu H, Guo X, Liu Y and Yuan Z. Preoperative prediction of perineural invasion and lymphovascular invasion with CT radiomics in gastric cancer. Eur J Radiol Open 2024; 12: 100550.

[20] Tanaka H, Hashiguchi K, Tabuchi M, Nessipkhan A, Akashi T, Shiota J, Kitayama M, Matsushima K, Yamaguchi N, Arai J, Kanetaka K, Nakashima M, Kudo T, Nakao K and Akazawa Y. (18)F-fluorodeoxyglucose positron emission tomography/computed tomography parameters are associated with histological outcomes in superficial esophageal squamous cell carcinoma. Sci Rep 2024; 14: 17493.

[21] Li Q, Feng QX, Qi L, Liu C, Zhang J, Yang G, Zhang YD and Liu XS. Prognostic aspects of lymphovascular invasion in localized gastric

cancer: new insights into the radiomics and deep transfer learning from contrast-enhanced CT imaging. Abdom Radiol (NY) 2022; 47: 496-507.
[22] Kim SJ, Choi CW, Kang DH, Kim HW, Park SB, Nam HS and Ryu DG. Preoperative predictors of beyond endoscopic submucosal dissection indication or lymphovascular invasion in endoscopic resection for early gastric cancer. Surg Endosc 2018; 32: 2948-2957.
[23] Lin JX, Wang ZK, Wang W, Desiderio J, Xie JW, Wang JB, Lu J, Chen QY, Cao LL, Lin M, Tu RH, Zheng CH, Li P, Parisi A, Zhou ZW and Huang CM. Risk factors of lymph node metastasis or lymphovascular invasion for early gastric cancer: a practical and effective predictive model based on international multicenter data. BMC Cancer 2019; 19: 1048.
[24] Oh YJ, Kim DH, Han WH, Eom BW, Kim YI, Yoon HM, Lee JY, Kim CG, Kook MC, Choi IJ, Kim YW and Ryu KW. Risk factors for lymph node metastasis in early gastric cancer without lymphatic invasion after endoscopic submucosal dissection. Eur J Surg Oncol 2021; 47: 3059-3063.
[25] Xue XQ, Yu WJ, Shao XL and Wang YT. Incremental value of PET primary lesion-based radiomics signature to conventional metabolic parameters and traditional risk factors for preoperative prediction of lymph node metastases in gastric cancer. Abdom Radiol (NY) 2023; 48: 510-518.
[26] Zhu H, Wang G, Zheng J, Zhu H, Huang J, Luo E, Hu X, Wei Y, Wang C, Xu A and He X. Preoperative prediction for lymph node metastasis in early gastric cancer by interpretable machine learning models: a multicenter study. Surgery 2022; 171: 1543-1551.
[27] Xue XQ, Yu WJ, Shi X, Shao XL and Wang YT. (18)F-FDG PET/CT-based radiomics nomogram for the preoperative prediction of lymph node metastasis in gastric cancer. Front Oncol 2022; 12: 911168.
[28] Ge HT, Chen JW, Wang LL, Zou TX, Zheng B, Liu YF, Xue YJ and Lin WW. Preoperative prediction of lymphovascular and perineural invasion in gastric cancer using spectral computed tomography imaging and machine learning. World J Gastroenterol 2024; 30: 542-555.

Table S1. The CT feature variables were filtered by lasso

variable	weight
original_shape_Sphericity.CT	0.451269435
log.sigma.3.0.mm.3D_ngtdm_Coarseness.CT	2.960767109
wavelet.LHH_gldm_SmallDependenceEmphasis.CT	-0.141650226
wavelet.HLH_glszm_GrayLevelVariance.CT	0.002438399
original_glszm_SizeZoneNonUniformityNormalized.CT	1.331090563
log.sigma.4.0.mm.3D_glcm_Contrast.CT	0.07606041
original_glszm_SmallAreaEmphasis.CT	13.31256998
wavelet.LHL_firstorder_Entropy.CT	0.014365532
wavelet.LLH_glcm_Idmn.CT	-0.348362421
wavelet.LLH_glszm_LargeAreaLowGrayLevelEmphasis.CT	-0.007743832
wavelet.HLH_firstorder_Kurtosis.CT	4.492034252
original_glcm_Correlation.CT	0.019309818
original_glcm_ClusterProminence.CT	-0.462714481
original_firstorder_Skewness.CT	6.640129682
wavelet.LHL_glcm_Contrast.CT	-4.19636E-05
wavelet.LLL_glcm_Imc1.CT	0.008845578
wavelet.HLL_glszm_LargeAreaHighGrayLevelEmphasis.CT	-2.391167812
log.sigma.2.5.mm.3D_glcm_Dissimilarity.CT	-6.022301129
wavelet.LLL_glszm_SmallAreaEmphasis.CT	-11.3729082
wavelet.HHL_gldm_DependenceEntropy.CT	-0.291766899
wavelet.HHH_glcm_ClusterShade.CT	1.339092137
wavelet.LHH_firstorder_Median.CT	-0.034970394
wavelet.LHL_glszm_LargeAreaEmphasis.CT	-2.578511172
wavelet.LHL_glcm_Idn.CT	-1.105948524
wavelet.HLL_glszm_HighGrayLevelZoneEmphasis.CT	0.002052111
wavelet.LHH_firstorder_Kurtosis.CT	0.080220315
wavelet.HLH_firstorder_Energy.CT	-0.101156592
wavelet.LHH_glszm_SizeZoneNonUniformityNormalized.CT	0.007451411

Table S2. The PET feature variables were filtered by lasso

variable	weight
wavelet.HHH_glcm_ClusterShade.PET	-1.647612368
wavelet.HLL_glszm_LargeAreaHighGrayLevelEmphasis.PET	0.585577283
original_glszm_SmallAreaEmphasis.PET	-1.584806561
original_glszm_SizeZoneNonUniformityNormalized.PET	-0.949995944
wavelet.LLH_glszm_LargeAreaLowGrayLevelEmphasis.PET	0.013887931
wavelet.LHH_glszm_SizeZoneNonUniformityNormalized.PET	0.120520629
wavelet.HLH_firstorder_Kurtosis.PET	1.813839574
log.sigma.3.0.mm.3D_ngtdm_Coarseness.PET	-1.77937138
wavelet.LHH_firstorder_Median.PET	-0.163115928
log.sigma.2.5.mm.3D_glcm_Dissimilarity.PET	-0.023021383
wavelet.LLL_glcm_Imc1.PET	-0.206481766
original_firstorder_Skewness.PET	0.425849364
wavelet.HLH_glszm_GrayLevelVariance.PET	0.600941031
wavelet.LHH_gldm_SmallDependenceEmphasis.PET	1.572385006

Table S3. The CT / PET feature variables were filtered by lasso

variable	weight
wavelet.HHH_glcm_ClusterShade.PET	-2.377105435
wavelet.HLL_glszm_LargeAreaHighGrayLevelEmphasis.PET	0.64071659
wavelet.HHL_glcm_Idn.PET	0.249045766
original_glszm_SmallAreaEmphasis.PET	-0.369968448
log.sigma.3.0.mm.3D_ngtdm_Coarseness.CT	0.978214558
wavelet.LHH_gldm_SmallDependenceEmphasis.CT	-0.143843241
wavelet.HLH_glszm_GrayLevelVariance.CT	0.001405012
original_glszm_SizeZoneNonUniformityNormalized.CT	1.353130597
original_glszm_SmallAreaEmphasis.CT	7.579289356
wavelet.LHL_firstorder_Entropy.CT	0.006726383
original_glszm_SizeZoneNonUniformityNormalized.PET	-1.381720385
wavelet.LLH_glcm_Idmn.CT	-0.194975259
wavelet.LLH_glszm_LargeAreaLowGrayLevelEmphasis.CT	-0.007176366
wavelet.HLH_firstorder_Kurtosis.CT	3.683144761
wavelet.LHH_glszm_SizeZoneNonUniformityNormalized.PET	0.772132618
wavelet.HLH_firstorder_Kurtosis.PET	3.089325336
original_firstorder_Skewness.CT	3.188204198
wavelet.LLL_glcm_Imc1.CT	0.013712976
wavelet.HLL_glszm_LargeAreaHighGrayLevelEmphasis.CT	-0.928407935
log.sigma.3.0.mm.3D_ngtdm_Coarseness.PET	-2.330698235
log.sigma.2.5.mm.3D_glcm_Dissimilarity.CT	-5.223945643
wavelet.LLL_glszm_SmallAreaEmphasis.CT	-8.900796857
log.sigma.2.5.mm.3D_glcm_Dissimilarity.PET	-0.027907699
wavelet.HHL_gldm_DependenceEntropy.CT	-0.087199486
log.sigma.4.0.mm.3D_glcm_Contrast.PET	-0.000484795
wavelet.HHH_glcm_ClusterShade.CT	1.212315196
wavelet.LHH_firstorder_Median.CT	-0.017543072
wavelet.LHL_glszm_LargeAreaEmphasis.CT	-3.345517292
wavelet.LLL_glcm_Imc1.PET	-0.110072218
wavelet.LHL_glcm_Idn.CT	-0.427666102
wavelet.HLL_glszm_HighGrayLevelZoneEmphasis.CT	0.001400157
wavelet.HLH_firstorder_Energy.CT	-0.0870774
wavelet.LHH_gldm_SmallDependenceEmphasis.PET	1.473854946